



# LUND UNIVERSITY

## Fast 4-D Imaging of Fluid Flow in Rock by High-Speed Neutron Tomography

Tudisco, Erika; Etxegarai, Maddi; Hall, Stephen; Charalampidou, Elli-Maria; Couples, Gary D.; Lewis, Helen; Tengattini, A.; Kardjilov, Nikolay

*Published in:*

Journal of Geophysical Research: Solid Earth

*DOI:*

[10.1029/2018JB016522](https://doi.org/10.1029/2018JB016522)

2019

*Document Version:*

Peer reviewed version (aka post-print)

[Link to publication](#)

*Citation for published version (APA):*

Tudisco, E., Etxegarai, M., Hall, S., Charalampidou, E.-M., Couples, G. D., Lewis, H., Tengattini, A., & Kardjilov, N. (2019). Fast 4-D Imaging of Fluid Flow in Rock by High-Speed Neutron Tomography. *Journal of Geophysical Research: Solid Earth*, 124(4), 3557-3569. <https://doi.org/10.1029/2018JB016522>

*Total number of authors:*

8

### General rights

Unless other specific re-use rights are stated the following general rights apply:

Copyright and moral rights for the publications made accessible in the public portal are retained by the authors and/or other copyright owners and it is a condition of accessing publications that users recognise and abide by the legal requirements associated with these rights.

- Users may download and print one copy of any publication from the public portal for the purpose of private study or research.
- You may not further distribute the material or use it for any profit-making activity or commercial gain
- You may freely distribute the URL identifying the publication in the public portal

Read more about Creative commons licenses: <https://creativecommons.org/licenses/>

### Take down policy

If you believe that this document breaches copyright please contact us providing details, and we will remove access to the work immediately and investigate your claim.

LUND UNIVERSITY

PO Box 117  
221 00 Lund  
+46 46-222 00 00

# Fast 4D imaging of fluid flow in rock by high-speed neutron tomography

E. Tudisco<sup>1</sup>, M. Etxegarai<sup>2</sup>, S. A. Hall<sup>3</sup>, E. M. Charalampidou<sup>4</sup>, G.D.  
Couples<sup>4</sup>, H. Lewis<sup>4</sup>, A. Tengattini<sup>2,5</sup> and N. Kardjilov<sup>6</sup>

<sup>1</sup>Division of Geotechnical Engineering, Lund University, Sweden

<sup>2</sup>Univ. Grenoble Alpes, CNRS, Grenoble INP, 3SR, F-38000 Grenoble, France

<sup>3</sup>Division of Solid Mechanics, Lund University, Sweden

<sup>4</sup>Institute of Petroleum Engineering, Heriot-Watt University, Edinburgh UK

<sup>5</sup>Institut Laue-Langevin (ILL), France

<sup>6</sup>Helmholtz-Zentrum Berlin (HZB), Germany

## Key Points:

- Full 3D fluid front velocity map can be obtained from high-speed (1 minute/tomography) neutron tomography during water invasion into air-filled samples
- Quantitative measurements are validated by comparing experimental results to 1D analytical solution of pressure-driven flow
- During imbibition, compactant shear bands result in locally higher fluid-flow velocity due to decreased pore size in the bands

---

Corresponding author: Erika Tudisco, [erika.tudisco@construction.lth.se](mailto:erika.tudisco@construction.lth.se)

## Abstract

High-speed neutron tomographies (one minute acquisition) have been acquired during water invasion into air-filled samples of both intact and deformed (ex-situ) Vosges sandstone. 3D volume images have been processed to detect and track the evolution of the waterfront and to calculate full-field measurement of its speed of advance. The flow process correlates well with known rock properties, and is especially sensitive to the distribution of the altered properties associated with observed localised deformation, which is independently characterised by Digital Volume Correlation (DVC) of x-ray tomographies acquired before and after the mechanical test. The successful results presented herein open the possibility of in-situ analysis of the local evolution of hydraulic properties of rocks due to mechanical deformation.

## 1 Introduction

Deformation in rocks is typically not homogeneous and is often localised into features such as shear or compaction bands. Such deformation can have significant influence on the hydraulic properties of the rock because it locally alters the rock structure in ways that are expected to change the local flow properties. Standard experimental approaches to assess deformation and changes in fluid flow in rocks are based on measurements of fluxes and pressures taken at the boundaries of a tested sample. These measurements, however, cannot provide information on internal heterogeneities, which likely exert a strong control on the mechanical and fluid flow behaviour. Therefore, understanding how rock deformation influences the hydraulic properties of rocks requires local observations that can provide a direct link between the mechanical deformation-induced changes and the altered fluid flow responses. This necessitates 3D observations of flow and measurements over time, since the fluid flow is a dynamic process that can only be assessed as it occurs, and deformation features can have a complex 3D arrangement. Thus, time-resolved 3D (i.e., 4D) measurements and observations are required.

X-ray imaging has become a common method to characterize the internal structure of bulk objects (e.g., Maire and Withers (2014)), including geomaterials, such as rocks and soils (e.g., Cnudde and Boone (2013)). Such 3D imaging has been extended to look at the evolution of localised deformation in rocks using time-lapse imaging and Digital Volume Correlation (DVC) (e.g., Charalampidou et al. (2013)). Water imbibition in rock specimens with compaction bands has also been studied using medical x-ray tomography (David et al., 2008; Pons et al., 2011) and pore-scale fluid flow processes have been imaged in small rock samples using 4D x-ray micro-tomography (Berg et al., 2014; Youssef et al., 2013; Pak et al., 2015). X-rays, however, have a strong interaction with the rock material and a much smaller interaction with the pore fluids of interest. Neutron imaging provides an alternative method that is much better adapted to the imaging of hydrous fluids in rocks. Neutrons have a different interaction mechanism with matter to x-rays. In particular, neutrons are absorbed or scattered by the nucleus of the atoms while x-rays interact with the electrons shells. Therefore, x-rays absorption is mainly proportional to material density whilst neutrons absorption is linked to the capacity of the nucleus to host an additional neutron. This leads to a strong interaction of neutrons with hydrogen, whose nucleus is formed by only a proton and it is keen to receive a neutron, and thus with the hydrogen-rich fluids of interest in rocks. In contrast, deuterium does not have such a capture site (it is already filled), and thus the  $D_2O$  form of water is substantially transparent to neutrons, much like the solid components of the rock and the metals used in the experimental configuration. (e.g., Perfect et al. (2014); Kaestner et al. (2016)). Therefore, much higher contrasts of fluid, compared to the rock, can be achieved with neutron imaging than with x-ray imaging, which enables much lower saturations to be detected. Furthermore, with a higher contrast, a sufficient signal to noise ratio can be obtained with a shorter acquisition time leading, potentially, to faster imaging.

Previous work (e.g., Masschaele, Dierick, Cnudde, et al. (2004), Masschaele, Dierick, Van Hoorebeke, et al. (2004), Hall (2013), Tötze et al. (2017), Tudisco, Hall, et al. (2017)) demonstrated the potential of neutron imaging to follow internal fluid flow in geomaterials. In Masschaele, Dierick, Cnudde, et al. (2004) and Masschaele, Dierick, Van Hoorebeke, et al. (2004) an example of 3D visualisation of fluid advanced is presented. However, the dimensions of the sample and the resolution were limited and no information on acquisition time is provided. The authors express the need for a quantitative analysis of the water front motion. In deformed rock samples, this analysis was restricted to 2D (radiography) imaging due to limitations with the possible acquisition speed. Here, the restriction to only 2D imaging of dynamic flow processes is overcome with advances in high-speed neutron tomography, to provide full 3D observations of flow processes that operate over a finite time interval. These measurements are analysed to provide full-field analysis of fluid-front velocity distributions, which is linked to hydraulic conductivity and the boundary conditions, for; (i) an intact rock sample subjected to pressure-driven flow; (ii) a sample exhibiting localised deformation subjected to a water-imbibition process. In the second case, the fluid flow analysis is compared with 3D measures of deformation from DVC.

## 2 Experimental approach

The neutron tomographies employed in this work were acquired with a high-speed imaging set-up at the CONRADII beamline at Helmholtz Zentrum Berlin (HZB) (Kardjilov et al., 2011), as described in the following. High-speed neutron imaging (1 minute per tomography) is possible at CONRADII using a white beam at the experimental position closest to the neutron guide, where the neutron flux is maximum (i.e.,  $2 \times 10^8$  n/cm<sup>2</sup>), which enables the exposure time to be minimized. However, at this position, the distance,  $L$ , between the pinhole aperture (diameter,  $D$ ), which defines the source, and the sample is small. Since the resolution for neutron imaging is defined by the ratio  $L/D$ , this implies a reduced spatial resolution. For the experiments presented here, a pinhole diameter of 30 mm was used, which gives an  $L/D$  ratio of 167. In addition to the  $L/D$  ratio, the distance,  $l$ , between the sample and the detector also influences the image resolution according to the equation  $d = l \cdot D/L$ , where  $d$  is the maximum blur (e.g., Banhart (2008)). Therefore, samples should be placed as close as possible to the detector; here, due to the sample diameter, this distance was 20 mm, giving a theoretical resolution of 120  $\mu$ m.

The neutron tomography acquisitions involved 300 radiographic projections acquired during rotation of the sample over 180°. Acquisitions were made with consecutive, continuous positive and negative rotations over 180°, as full rotation over 360° was not possible due to the possibility of collision between the detector and the water inlet tube (see Fig. 1). To minimise the exposure time for each projection the camera was used with a pixel binning of 4x4 pixels. This allowed fast exposures (0.2 s per projection) with sufficient signal:noise, which, in turn, permitted continuous rotation, without deadtime for stopping for each projection. With these settings, the full tomography acquisition of 300 projections could be acquired in just 1 minute and with a pixel size of 100  $\mu$ m over a field of view (FoV) of about 60x73 mm<sup>2</sup>, which is slightly smaller than the height of the samples. (Note that, due to the high attenuation by the silicone used to seal the base of the sample cup, the useable FoV was slightly smaller vertically).

Two samples have been studied in this work to illustrate the experimental approach. These were both 38 mm diameter cylindrical samples of arkosic Vosges sandstone (22% porosity) selected from the materials used in Charalampidou et al. (2011, 2013). One sample (IGSN: IEETV003) was “as-cored” and the other (IGSN: IEETV002) had been loaded under triaxial conditions at 30 MPa confining pressure such that it contained shear bands. A notch was cut at about 2/3 of the height of the sample and covering 1/4 of the circumference to encourage the expected localised deformation to occur in the middle

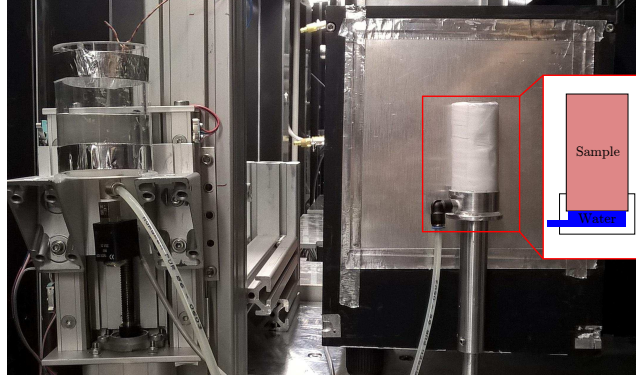


**Figure 1.** Photograph of the experimental set-up and a sketch of the inside of the cup. The water reservoir is to the left and the sample, mounted on the rotation stage, is to the right, in front of the scintillator of the detector. The electro-valve is visible below where the tube exits the reservoir. The metal post below the sample is attached to the rotation stage (out of sight, below).

region of the sample, similarly to Charalampidou et al. (2011)). This deformed sample had been imaged before and after the triaxial testing using both x-ray and neutron tomography. DVC was performed on the x-ray images using the code TomoWarp2 (Tudisco, Andò, et al., 2017) to provide 3D volumetric and shear strain maps throughout the sample that are used here to compare to the flow measurements. This analysis indicated that two main shear bands had developed extending from the notch, one reaching the top of the sample and the second extending diagonally downward for about 25 mm. Additional, mainly smaller (shorter), bands occur in complex patterns that are associated with the larger bands, or they may be located away from it. Although the orientations of these smaller bands are mainly similar to the main bands, there are differences that lead to a reluctance to describe the entire array as having variations only in two axes.

The intact sample had parts of the cylindrical sides removed to create two, diametrically-opposite flat faces on which two notches had been cut on the surfaces at different heights. This particular shape enables further advanced measurements (i.e., ultrasonic tomography) to fully characterise the sample before and after deformation. For the neutron experiments (to ensure a good fluid sealing and optimal imaging), specially machined teflon inserts were placed on the flat surfaces to recover a cylindrical shape. Teflon tape was wrapped around the sample before the inserts were positioned to prevent fluid from being able to flow out of the sides of the sample. The sample, plus teflon inserts, was confined in a heat-shrunk Fluorinated Ethylene Propylene (FEP) membrane to seal the ensemble. The complete sample assembly was mounted and sealed with silicone onto a specially-designed end-cup, which allows water to contact the entire sample base. This cup was connected by flexible tubing to a small reservoir on a table whose height could be remotely adjusted (see Figure 1). An electro-valve, controlled from outside the experimental area, allowed the fluid supply from the reservoir to the end-cup to be turned on or off.

During the first test, on the intact sample, the level of the water was kept at a constant height, above the top of the sample, by moving the reservoir upwards to compensate for the fluid leaving the reservoir and entering the sample. In this way, an almost-constant water pressure was applied at the bottom of the sample. For the initial stage of the second test (sample with shear bands), the level of the water was kept constant and level with the top of the sample to accelerate the advance of the fluid until the wa-

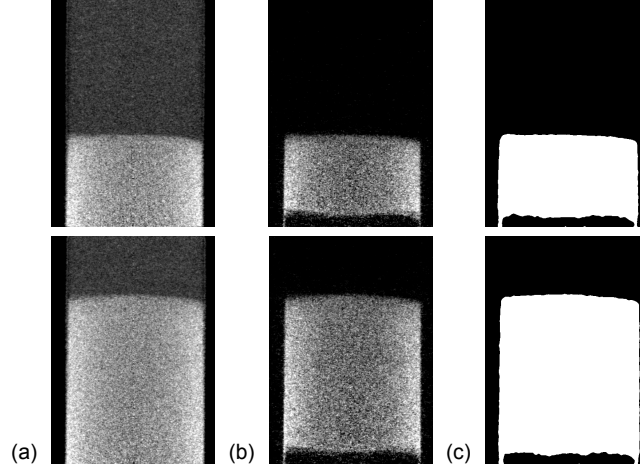


**Figure 2.** (a) Two vertical cross-section slices through the high-speed neutron tomography images of the intact sample at different times in the fluid flow process. (b) The same slices reconstructed after subtracting the initial (dry) images, as described in the text. (c) Corresponding slices through the binarisation of (b). Note that the first (dry) tomography was made when water was already in the field of view, so the region of the sample where water was already present appears as a dark area at the bottom of the image in (b) and (c).

ter front reached about 1/3 of the sample height. Subsequently, the reservoir was lowered to maintain the water level a few mm above the sample base, which allowed imbibition-dominated flow to be studied in the area of the sample that presented localised deformation (middle-top part). The flow experiments lasted for about 2.5 hours for the intact sample and 5.5 hours for the deformed one, which resulted in 149 and 384 tomographies, respectively. A technical problem occurred in the middle of the second test such that no images were acquired for about 40 minutes, which resulted in a gap in the imaging of the imbibition process.

### 3 Image analysis

The tomographic reconstructions were performed using an in-house Python code based on the ASTRA tomography toolbox (van Aarle et al., 2015; W. J. Palenstijn et al., 2017) assuming a parallel beam and using the 3D SIRT GPU-based algorithm (W. Palenstijn et al., 2011). Figure 2(a) presents two vertical slices extracted from the centre 3D images of the intact sample at two different times. These images clearly show the advance of the fluid front and the imaged texture of the rock in the dry region above the advancing front. In the water-filled area, the neutron attenuation is high and the textural information is obscured. Moreover, a beam hardening effect is evident in the saturated region. To facilitate the thresholding of the images described above, the tomographic reconstruction was repeated using radiographic projections normalised with the corresponding projections from the initial tomographic scan of the dry sample. This procedure allowed only the water to be reconstructed, as shown in Figure 2(b). It can be seen that this process removes the rock sample texture from the images, which provides further support that the sample texture visible in Figure 2(a) is real and not noise.

The focus of these experiments is to demonstrate the capability to achieve a quantification of the advance of the fluid front, which is clearly visible in the images in Figure 2. The contrast between the fluid-filled and the dry regions of the samples is much greater than the noise level or the effect of beam hardening, especially after removing



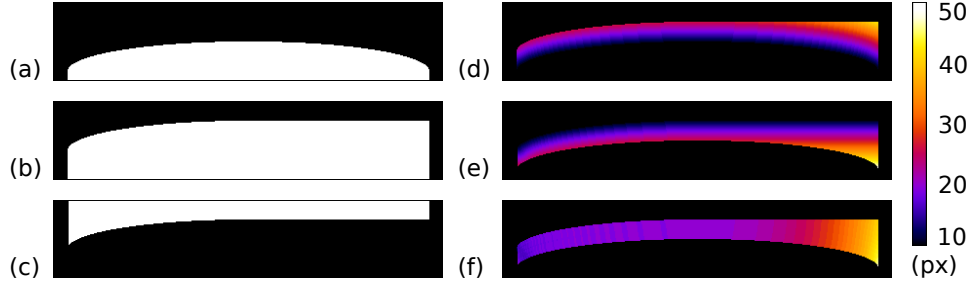


**Figure 3.** Speed field determination steps: binary image of (a) the initial front (Front 1) and (b) the manually-adjusted next front (Front 2), (c) negative of Front 2, distance map from (d) Front 1 and (e) from Front 2 masked to show only the area of interest, (f) sum of the distance maps.

the tomographic images of the dry sample (Figure 2(b)). By binarisation of the 3D images it is possible to separate the dry and wet volumes to provide a series of binary 3D images that represent a time series of the water front progression. From each consecutive pair of binary image series, a 3D map of the speed of advance of the water front has been calculated, as described in the following.

Figure 3 illustrates the speed map determination approach for an artificial 2D case with a front manually moved up 20 pixels in the vertical direction and flattened on one side so that the maximum displacement there is 48 pixels. The first step in the analysis procedure involves calculation of the euclidean distance of each pixel in the image from the nearest black pixel to give distance maps. This is performed for the first binary image in each consecutive image pair and is repeated for the second image in the pair, but with a negative of the binarised image to retrieve the distance in the correct direction from the second front (i.e., downward). To reduce artefacts at the boundaries of the sample, the outside of the sample in the images was set to zero (see Figure 3(c)). For the real data, the shape of the sample is determined from the last tomography image, when the sample is full of water. The two distance maps are subsequently masked to retain only the image of the sample region between the two fronts. These masked distance maps are summed together to provide a new image that represents, for each point in the image, the shortest-path distance that water crossing the point travels to reach the second front from the first. Knowing the time elapsed between the acquisition of the two images, this distance can be directly converted to a speed of the front advance for each point between the fronts in the pair of images. Figure 3(f) shows that the calculated distance, in the artificial example, is constant and equal to 20 px where the front has moved uniformly, whereas the distance increases where the front is distorted. Curvature of the front at the boundaries results in an inclined path being shorter than the vertical one. Whilst this does not correctly represent the imposed constant advance of the front and indicates caution should be applied when interpreting the boundary areas, this might be considered as a reasonable representation of a real flow where there is no reason for the water to advance only in the vertical direction.

The described procedure provides the “instantaneous” flow speed field of the advance of the water-front between two tomographies. Repeating the process for each consecutive pair of images and assembling the results provides a full speed map volume covering the entire imaged sample. The resolution of the speed map is determined by the frequency of the front reconstructions (each tomography) and it is limited by the noise, which affects the smoothness of the surface. To obtain reasonable results, the movement between two fronts has to be larger than the front roughness.

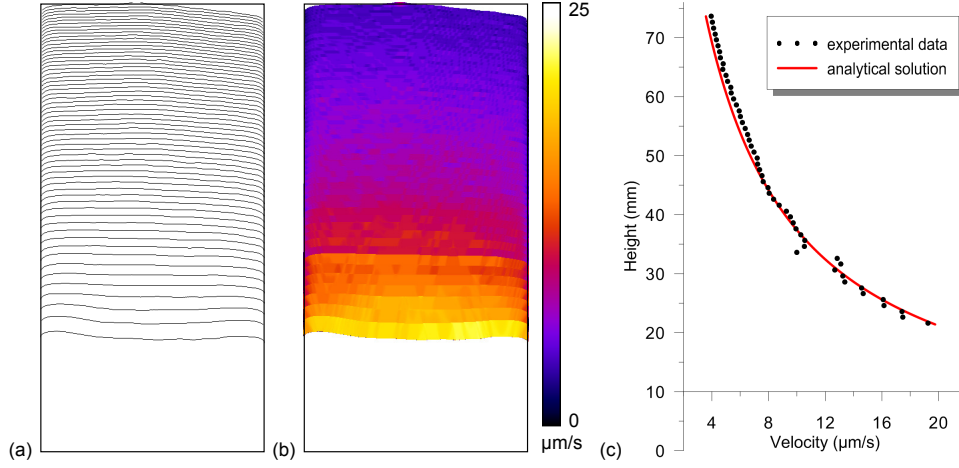


**Figure 4.** (a) A series of waterfronts in the central vertical slice, (b) corresponding vertical slice of the water speed map for the intact sample, and (c) an analytical solution, as in equation (1), fitted with experimental data.

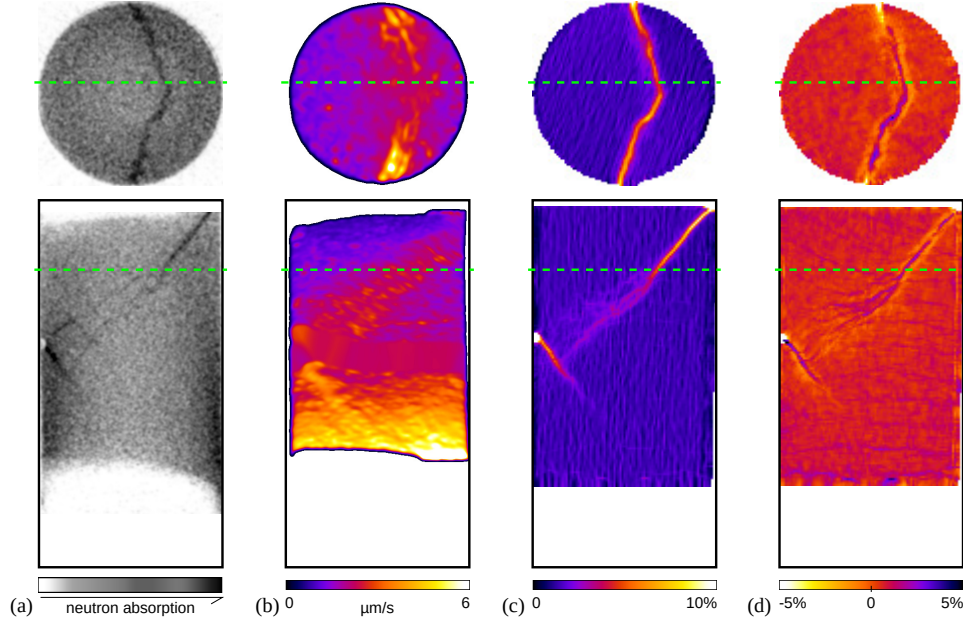
## 4 Results

Figure 4 shows, for the intact sample, the positions of the water-fronts (at 2 minute intervals) in a vertical central slice through the imaged volume and the corresponding slice through the 3D speed map (the former determined by binarisation of the tomography images during the water advance, and the latter calculated using the method described above). The speed map shows a decrease in the speed of the front advance with increasing height of the front. This is consistent with a decreasing pressure gradient with increased distance of the front from the constant-pressure condition at the sample base. Furthermore, the flow-speed field does not show any significant local variations, which is as expected from the assumption of a nominally intact and quasi-homogeneous sample. Moreover, closer inspection of the fluid front in the tomography images indicates there is no significant gradient in saturation at the front. Therefore, the role of capillarity effects can be neglected in the analysis: i.e., the flow is predominantly pressure driven.

The second test differs from the one described above in two respects: it contains an array of experimentally-created deformation bands; and the flow experiment is conducted so that, in the top part of the sample, imbibition of water is the only operative driving force. Figure 5 shows horizontal and vertical slices through: (a) the neutron tomography image at the end of the flow experiment; (b) the water-front speed volume; (c-d) the maximum shear- and volumetric-strain volumes derived from DVC applied to x-ray tomographies acquired before and after triaxial deformation. Strain localisation bands, and their related flow effects, are clearly visible in all the presented images, including the smaller scale features of the localised deformation in the upper part of the sample. Figure 6 presents the 3D rendering of the water speed map and the maximum shear strain, in which low values are displayed as transparent to allow the visualisation of the deformation band. The images show the variability of the deformation along the sample in both shape and intensity. Such variability would be lost in a 2D analysis, where only an average projected value in the plane of the deformation can be measured.

The higher attenuation of neutrons seen in the region of the deformation bands in Figure 5(a) indicates higher water saturation, and the water-front speed map (Figure 5(b)) shows a higher value inside the bands. This experiment was conducted so that imbibition of water is the only operative driving force, therefore the higher speed in the localised deformation bands can be interpreted as being related to higher air-water cap-





**Figure 5.** horizontal and vertical slices through: (a) the neutron tomography image at the end of the flow experiment; (b) the water speed volume; (c) the maximum shear-strain volume; (d) volumetric-strain volume (positive values indicate compression). The strain fields were derived from DVC applied to x-ray tomographies acquired before and after triaxial deformation. To better highlight the variations in the water speed map, a Gaussian filter with radius 5 pixels was applied twice to enhance the signal:noise) this also generates the dark borders visible in (b)).

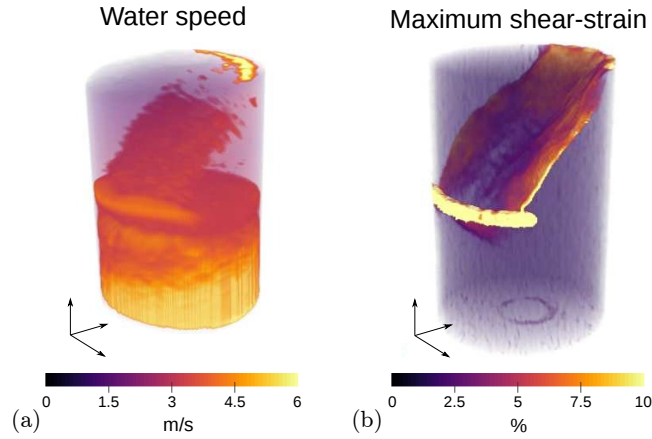


**Figure 6.** 3D rendering of (a) the water speed map and (b) the maximum shear strain. Low values are displayed as transparent to allow the visualisation of the deformation band.

illary pressure, which suggests smaller pore sizes in the band than in the surrounding region. This hypothesis is consistent with the strain maps from the DVC, which reveal that the shear bands are predominantly compactant (although some regions of dilation can also be seen, especially close to the boundary of the sample). The shear band extending downwards from the notch shows higher water-front speeds, which suggests that the capillary properties in this part of the band array are strongly affected by deformation, even though this localisation zone is less visible in the DVC results. In contrast, the band continuing from the notch towards the top of the sample appears to have a lesser impact on the water speed, compared to the surrounding region. This could be due to the much lower velocity of the water at this height (which can only advance as quickly as more water can arrive from below), which would make the difference between the velocity in the band and in the surrounding area too small to be appreciated. Another possible explanation is the dilatant character of this part of the shear band, which might reduce the capillary effects. In the central height region, where no information is available on flow because of the break in the image acquisition described above, it is interesting to note that the method is still able to capture the average speed and the higher speed in the bands despite the long distance between the two water-fronts.

An additional neutron experiment is briefly described here to emphasise the relevance of the three-dimensional nature of tomography. This experiment is performed on a carbonate (limestone) rock comprised of very thin layers (called laminae, <1mm thick) oriented orthogonal to the cylinder axis. These laminae are composed of aggregates of micro-crystals (2-5  $\mu\text{m}$  diameter), with alternating laminae exhibiting variations in inter-crystalline pore space such that local porosity ranges from <15% to >45% (Buckman et al., 2018). The sample was pre-deformed (dry) to just past the peak stress at a confining pressure of 20 MPa. Instead of developing through-going deformation bands like the samples described above, it developed a complex array of shorter, planar and predominantly steep features (Figure 7(a)) that exhibit a dilational (lower density) character on x-ray tomography examination (Figure 7(d)). On subsequent inspection by SEM (Scanning Electron Microscopy), they are seen to include a dilation-dominant mixture but with some compactional zones (Figure 7(b),(c)). Nominally, at macro-scale, these features look like partly-open fractures, with shear movement indications as well as openings like those seen at smaller scale in the SEM images. They are typically steeply inclined with multiple orientations arrayed around the sample axis, and altogether, they create a complex network of partially-intersecting discontinuities at a wide variety of orientations that cannot be captured in a 2D representation (Figure 7(e),(f)). They also exhibit a clear relationship with the laminae, with terminations typically but not exclusively occurring at lamina boundaries.

The neutron experiment on this sample (performed at the Institut Laue-Langevin (ILL), using the then newly-commissioned NeXT facility, which at the time could not acquire high-speed neutron tomographic images due to constraints, since overcome, with the control software for the rotation stage) reveals considerable complexity in the flow patterns. The initially air-filled sample was subjected to slow water injection at its base, using a cup analogous the one described above. The invasion of the initial fluid ( $\text{D}_2\text{O}$ ) was extremely non-uniform. The following description is based on neutron radiography images (Figure 8), so, while the observations reveal clear patterns of flow behaviour, the fixed viewpoint inevitably results in significant uncertainty except when the view is aligned directly along a planar feature. In particular it is impossible to identify if a tabular zone, or an irregular zone with finite length and width, as seen on the radiography is actually water in porous rock or if it is a fracture oriented normal to the viewing direction.

Initially, the water moved up along a few of the fractures, readily identifiable in the radiography as such (Figure 8(a)) because of their suitable orientation. These fractures were known to intersect the base. As well as moving up the fractures the  $\text{D}_2\text{O}$  moved horizontally creating a set of typically approximately tabular zones. These

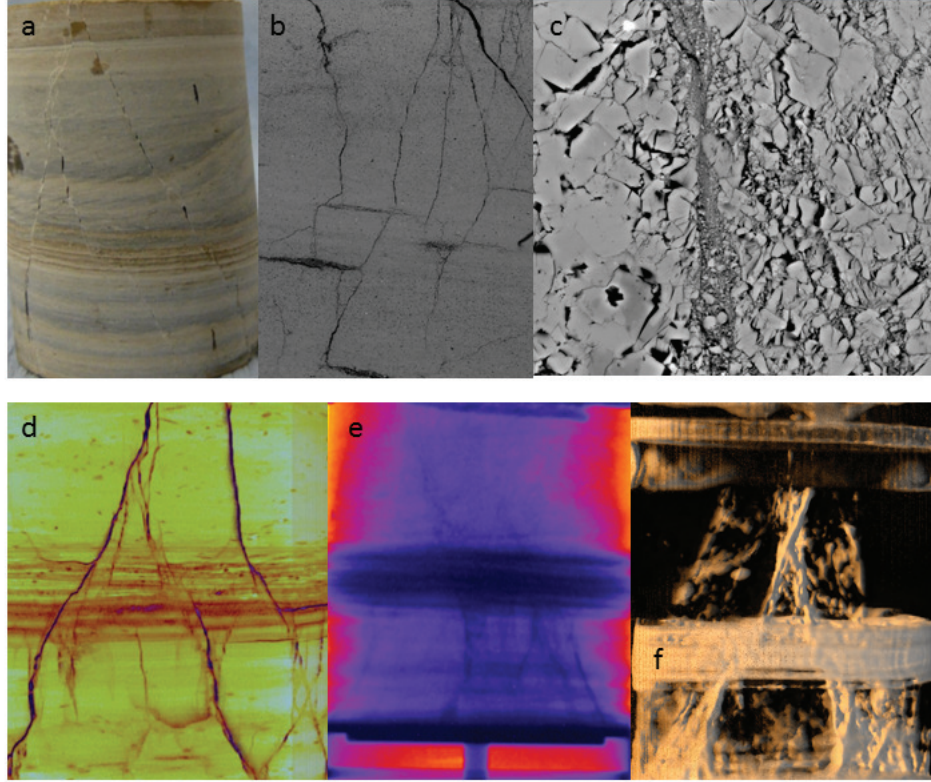


**Figure 7.** (a) Photo of deformed sample, showing laminated character of this rock, and the expression of deformation features as they intersect the sample exterior. Sample is 38mm diameter. (b) SEM image of a small ( $\sim 2$ mm field of view) part of the deformed sample. Image courtesy of Jim Buckman. (c) High-resolution SEM image of part of one fracture, showing the comminution of grains forming a groundmass of ultra-fine particles with nano-porosity. Note also the presence of disconnected microfractures within the band. Field of view  $\sim 20$  microns. Image courtesy of Jim Buckman. (d) Vertical slice from post-deformation x-ray tomography scan, showing that the fractures are dark (less dense). Note how some of the deformation features terminate against a depositional interface, and others transect larger regions. (e) Radiograph of the sample after significant water has entered the sample. Note how the fractures are dark, indicating higher water saturations. (f) Part of a 45-minute tomography scan obtained after  $\text{H}_2\text{O}$  replaces  $\text{D}_2\text{O}$ . Note how the  $\text{H}_2\text{O}$  is mainly located within the deformation features, but has invaded the unusual set of more porous laminations in the middle of the sample (compare also with (a) and (d)).

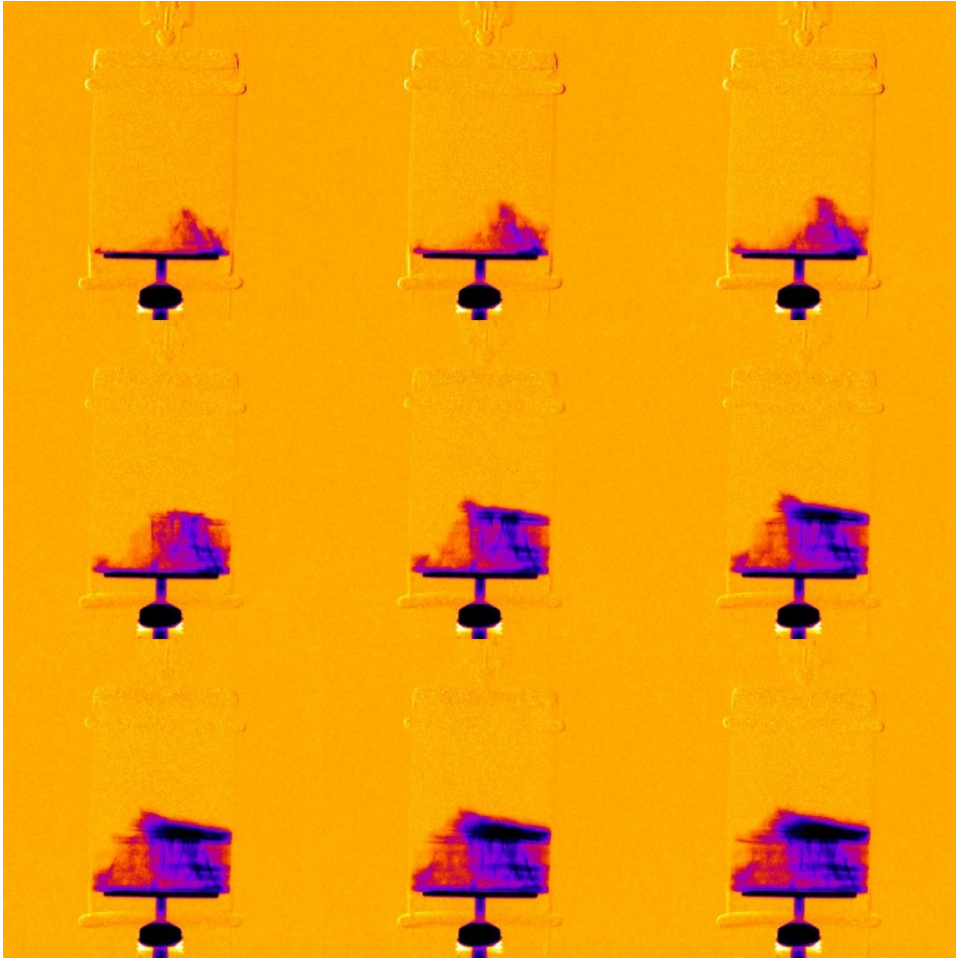


**Figure 8.** Sequential false colour radiographic images of the laminite sample.



semi-tabular zones show water ingress into laminae (Figure 8(b),(c)) but it was not possible to determine from the radiography if these zones were actually indicating D<sub>2</sub>O occupying the porespace of the undeformed rock or if it was occupying a fracture oriented at right angles to the direction of view. But the tomographic images (Figure 7(f)) show no open fractures in this position. Significant D<sub>2</sub>O saturation was normally achieved at least the right side of the sample as viewed in Figure 8 before the process moved to a progressively higher lamina and repeated. Generally filling moved from right to left, which was also away from the well-connected fracture network horizontally along the laminae, as well as from the base upwards. Some laminae were not invaded, while a few laminae were filled by cross-layer movement from an adjacent or nearby lower lamina: again this discrimination between lamina and fracture D<sub>2</sub>O ingress required the tomographic images. Some suitably oriented fractures can be seen in the radiography to start participating in the flow, and delivered D<sub>2</sub>O to a higher laminae, with the D<sub>2</sub>O then moving downwards into a dry lamina, typically along a fracture (compare Figure 8(c) and (d)): again the unsuitably oriented fractures needed the tomographic image to confirm their identity. This filling process was modified as the height of the D<sub>2</sub>O invasion increased, first encountering a zone of more porous laminae, with no suitably positioned open fractures, which filled (probably radially) lamina by lamina. The early stages of this process are seen in Figure 8(d). Above this region of more porous laminae, the sample has fewer but longer and less-well-connected fractures (Figure 7(f)). However the same pattern of water ingress along fractures and laminae was observed and confirmed by the combination of radiography and tomographic images as needed. When the invasion achieved a quasi-static state (i.e., no discernible changes in saturation), the injection fluid was switched to H<sub>2</sub>O. Due to higher neutron attenuation of H<sub>2</sub>O, the flow pattern in this semi-saturated condition was readily apparent (Figure 7(c)). During this phase of the experiment, the flow was almost exclusively concentrated within the fractures, and water exited the top of the sample very quickly.

Despite the high neutron flux ( $8.6 \times 10^7$  n/cm<sup>2</sup>/s), the initial setup on the NeXT facility (at the time this sample was used in the experiment) did not permit the rotation stage to operate at high-speed, so slower, higher quality tomographies (typically 45 minutes) were acquired. Fluid injection was stopped while individual tomographies were acquired, with a limited degree of diffusion taking place during the suspended flow. For the majority of the experiment, the process was only followed through radiography (with an exposure time of 0.6 s). However, at the more interesting points, the sample was remotely rotated to allow the experimental team to construct a mental picture of the 3D character of the flow being observed. For both tomography and radiography a pinhole of 20 mm was used, which gave an L/D of 500. The high-speed neutron tomographic method described here is now operational at the ILL, and achieves tomography acquisition in less than 1 minute, thanks to the uniquely high neutron flux. Subsequent experiments, using samples similar to this one, along with other carbonate rocks, have since been undertaken, and the full analysis of that suite of experiments will be reported separately. The key point, in relation to this paper, is that flow processes is intrinsically three-dimensional and can exhibit major complexity depending on the nature of the rock and its loading history. High-speed neutron tomography is in this respect an essential tool which enables new investigations of fluid flow in complex geomaterials.

## 5 Discussion

The results presented in the previous section demonstrate the ability to capture the time-dependent evolution of the fluid flow front in 3D via high-speed neutron tomography, both under pressure- and capillary-driven flow, and for a nominally homogeneous sample and a heterogeneous one that contains localised deformation features. Based on these results some clear questions might be posed, such as: (i) are the speed measure-

ments truly quantitative and reliable; (ii) how fast can the flow be and still be captured by this method?

To answer the first of the above questions, a comparison against an analytical solution can be made for the first test on the intact sample, as, in this case the water fronts are sub-horizontal, which allows the system to be considered as 1-dimensional. On this basis, Darcy's law defines a linear relationship  $q = -Ki$ , where  $q$  is the specific discharge,  $K$  is the hydraulic conductivity,  $i$  is the hydraulic gradient, with  $i = (h_1 - h_2)/z$  where  $z$  is taken as the height of the wetted area of the experiment, and  $h_1$  and  $h_2$  are the hydraulic head values at the bottom and top of that region. The pressure (head) at the bottom of the sample is constant and given by the water-tank level ( $z_w$ ). Setting  $z = 0$  at the bottom of the sample, the hydraulic head is  $h_1 = z_w = 160\text{mm}$ . The pressure at the water-front is zero and the hydraulic head is  $h_2 = z$ . The hydraulic gradient changes with time because the height of the wetted region increases and the specific discharge, which is equivalent to a flow speed, is given by:

$$q(z) = -K(1 - z_w/z). \quad (1)$$

Given the flow speed determined for each height in the sample, a value for the parameter  $K$  can be determined, from which the permeability of the sample,  $k$ , can be derived by  $k = K\mu(\rho g)$ , where  $\mu$  and  $\rho$  are the water viscosity and density, respectively. The analytical equation (1) has been fitted to the experimental points obtained by averaging the water speed values over square horizontal slices in the middle of the sample, avoiding the edge effects, see Figure 4(c). Fitting of (1) to these data provides a best-fit value for  $K$  of  $3.3 \times 10^{-6}$  m/s, which corresponds to an apparent permeability of  $3.3 \times 10^{-9}$  cm<sup>2</sup>, which compares well with lab-measured values of 1–2 Darcy obtained with other samples of this sandstone. The good fitting of the curve and the realistic value found for the permeability suggests that the hypothesis of pressure driven flow is correct and that the results from this imaging method can be used for quantitative analysis.

With respect to the second question above, accepted wisdom suggests that, in general, changes in a sample being imaged for tomographic reconstruction should not exceed one pixel during the scan to allow a good reconstruction of the volume. In this case, the analysis provided reasonable results even where the water-front was moving around 1 mm per minute (i.e., 10 pixels advance of the front during the time taken for the tomography data to be acquired). The movement of the water, however, causes a distortion in the reconstructed volume since the front is lower in the first projection than in the last one. For this reason, measurements of the frontal advance speed are best made between even numbers of tomographies (i.e., with the same rotation direction) to have the same kind of distortion in all the fronts. This issue can be overcome, in part, by analysing the data as a time-series of projections and not as reconstructed tomographic volumes, as has, for example, been described by Jailin et al. (2018).

In other tests not shown in this paper, it appears that, during imbibition, the water is always faster inside the deformation bands regardless of the confining pressure applied during the prior triaxial loading (which might be considered to control the characteristics of the resulting deformation). It is, however, crucial to carry out pressure-controlled flow tests with pre-saturated samples to study the effect of deformation on the local intrinsic permeability. Such tests have already been performed, but with only radiographic (2D) imaging of the sample during flow by Tudisco, Hall, et al. (2017), using a D<sub>2</sub>O (heavy water) saturated sample with pressure-driven H<sub>2</sub>O to replace the D<sub>2</sub>O. As D<sub>2</sub>O and H<sub>2</sub>O have very similar physical properties, but quite different neutron interactions (D<sub>2</sub>O attenuates neutrons much less than H<sub>2</sub>O), this can be considered as a single phase flow system where, as demonstrated by Tudisco, Hall, et al. (2017), it is possible to distinguish an advancing front (between H<sub>2</sub>O and D<sub>2</sub>O). Moreover, the tests of Tudisco, Hall, et al. (2017) were performed in-situ (i.e., during loading), placing a triaxial cell in the beamline, which enabled the study of the effects of evolving deformation and without unload-



ing or desaturation of the sample for the imaging. The results in this current work have shown that it is now possible to perform the 3D imaging sufficiently fast and to control the flow to be able to follow the flow processes in full 3D.

The fluid flow conditions used for these experiments, although not ideal to study intrinsic permeability, provide opportunities to make observations leading to important insights. An example is the situation depicted in Figure 6, where the water has preferentially moved upwards, above the general level of water and beyond the position of the notch, along the inclined shear band. The water front is still advancing along the band, while the water located within the band, but behind the front, is also continuing to move at high speed. The rock texture inside the band (based on examination of other Vosges samples deformed in the same campaign, and destructively sampled for thin sections and SEM studies) is believed to consist of a zone of broken grains, with smaller pore spaces between the fragments as compared against the texture of the intact rock. That texture is expected to result in high capillary pressure values within the band. The fast movement of water, as observed, is consistent with the inferred zone of higher capillary pressure. But why does the water behind the front continue to move at a rapid rate? Capillary pressure is an extremely local phenomenon, and is rooted at the pore scale, where the curvature of the water/air interface (in this example) provides the fluid energy that becomes expressed as an equivalent (negative or suction) pressure. Is it sensible to infer that the frontal advance pulls water along behind it? The answer is no, of course, and the physics of water movement in the already partly-saturated band has to be examined for another explanation.

It is possible to erect a working hypothesis that remains focused on capillary forces. The quasi-planar (but finite-thickness) band may well have a distribution of textures across its area. Some local spots could have smaller pore sizes, and thus higher effective capillary pressures. These would locally imbibe any water available from nearby regions, seeking to achieve a higher water saturation that would reduce the local energy differentials. So, there are plausible mechanisms for flow within the band. But the real question is not answered, because if local regions imbibe water from adjacent local regions, those source regions experience de-saturation, which introduces new energy differentials that counter the imbibition flow. Thus, the observed continuity of water in the partly-saturated band, and the persistence of rapid flow within it, implies that the band becomes a favored flow route. This reasoning leads to the hypothesis that the band also possesses a higher-permeability, as well as its higher capillary pressure. Higher permeability is usually thought to anti-correlate with higher capillary pressure, but the detailed flow observations provide a basis for supposing that the two characteristics exhibit a positive correlation. The same implications arise from consideration of the flow behaviour of the complexly fractured sample depicted in Figure 7, which will be treated in a subsequent paper focused on that sample suite.

The value of time-resolved 3D images of fluid flow, in rock samples with internal heterogeneities, is clear. The images provide evidence of flow processes that reveal complexity in the way that invading fluids move into the rocks, and the way that fluid moves in a saturated sample. In the case of the limestone sample, the experiment involved introduction of a contrasting fluid ( $\text{H}_2\text{O}$  replacing  $\text{D}_2\text{O}$ ), and the resulting flow pattern shows that the later fluid movement is focused in the planar deformation features that were previously thought to be simple opening-mode fractures. Current work is examining the local textures of these planar features, via destructive sampling that has enabled thin sections to be made and studied (e.g., as in Figure 7 (d)). Digital-rock methods are being applied to the textural images to derive local flow properties (Jiang et al., 2017, 2018). These will be assembled into whole-sample models that should provide a basis for developing a full process explanation of the fluid flow processes that can be observed via high-speed neutron tomography.

## 6 Conclusions

This paper has presented a new method, involving high-speed neutron imaging and image analysis, for 3D monitoring of fluid advance in rock specimens, with unprecedented spatio-temporal resolution. The new analysis method allows the determination of fluid-front advance speed at each voxel position in the 3D volume.

Quantitative full-field determinations of fluid-front speeds have been made in two samples of a sandstone, a nominally-intact specimen and one containing localised deformation features resulting from laboratory triaxial loading, for flow under pressure- and capillary-driven conditions, respectively. Verification of quantitative speed measurements has been performed by comparison to a 1D analytical model of pressure-driven flow for the intact sample, for which an hypothesis of homogeneity is reasonable. This verification provides confidence in the local measurements of capillary-driven fluid-front advance in the sample containing localised deformation features. The resultant fluid-front speed map for the deformed sample has been compared to full-field strain measurements from DVC analysis of x-ray tomography images acquired before and after the laboratory triaxial loading. This comparison reveals that the localisation of fluid-front speed correlates well with localisation of deformation and that the fluid-front advances faster in the more deformed regions of the samples (i.e., in the shear-bands). The apparent 'pull' of water in these bands likely relates to increased capillary drive relating to reduced pore-sizes, which is consistent with the general compactant nature of the localised shear features.

Based on the methods presented herein, it is now possible to perform 3D imaging sufficiently fast and to control the flow to be able to follow flow processes in full 3D and in-situ in a neutron imaging station. The next step is to combine this with in-situ triaxial loading and high spatial resolution time-lapse tomography to enable DVC analysis, which, combined with the 3D flow quantification of this paper, will enable studies of the evolution of both the deformation and the fluid flow, thus enabling research in hydro-mechanical coupling.

## Acknowledgments

Data supporting the conclusions can be obtained at [https://figshare.com/projects/Mechanical\\_deformation\\_and\\_fluid\\_flow\\_analysis\\_in\\_geomaterial/37097](https://figshare.com/projects/Mechanical_deformation_and_fluid_flow_analysis_in_geomaterial/37097)

## References

- Banhart, J. (2008). *Advanced tomographic methods in materials research and engineering* (Vol. 66). Oxford University Press.
- Berg, S., Armstrong, R. T., Ott, H., Georgiadis, A., Klapp, S. A., Schwing, A., ... Stampanoni, M. (2014, 7). Multiphase Flow in porous Rock Imaged with Fast X-ray Computed Micro-Tomography. In *1st international conference on tomography of materials and structures* (p. 223). Ghent (Belgium).
- Buckman, J., Charalampidou, E.-M. C., Zihms, S., Lewis, M. H., Corbett, P. W. M., Couples, G. D., ... Huang, T. (2018). High-resolution large area scanning electron microscopy: an imaging tool for porosity and diagenesis of carbonate rock systems. *Carbonate Pore Systems: New developments and Case Studies*, 112. (in press)
- Charalampidou, E.-M., Hall, S. A., Stanchits, S., Lewis, H., & Viggiani, G. (2011, 4). Characterization of shear and compaction bands in a porous sandstone deformed under triaxial compression. *Tectonophysics*, 503(1-2), 8-17. Retrieved from <https://www.sciencedirect.com/science/article/pii/S0040195110003938> doi: 10.1016/J.TECTO.2010.09.032
- Charalampidou, E.-M., Hall, S. A., Stanchits, S., Viggiani, G., & Lewis, H. (2013,

- 1). Characterization of Shear and Compaction Bands in Sandstone Using X-Ray Tomography and 3D Digital Image Correlation. In *Advances in computed tomography for geomaterials* (pp. 59–66). Hoboken, NJ, USA: John Wiley & Sons, Inc. Retrieved from <http://doi.wiley.com/10.1002/9781118557723.ch7> doi: 10.1002/9781118557723.ch7
- Cnudde, V., & Boone, M. (2013, 8). High-resolution X-ray computed tomography in geosciences: A review of the current technology and applications. *Earth-Science Reviews*, 123, 1–17. Retrieved from <https://www.sciencedirect.com/science/article/pii/S001282521300069X> doi: 10.1016/J.EARSCIREV.2013.04.003
- David, C., Menéndez, B., & Mengus, J.-M. (2008, 8). Influence of mechanical damage on fluid flow patterns investigated using CT scanning imaging and acoustic emissions techniques. *Geophysical Research Letters*, 35(16), L16313. Retrieved from <http://doi.wiley.com/10.1029/2008GL034879> doi: 10.1029/2008GL034879
- Hall, S. A. (2013, 6). Characterization of fluid flow in a shear band in porous rock using neutron radiography. *Geophysical Research Letters*, 40(11), 2613–2618. Retrieved from <http://doi.wiley.com/10.1002/grl.50528> doi: 10.1002/grl.50528
- Jailin, C., Etxegarai, M., Tudisco, E., Hall, S., & Roux, S. (2018). Fast Tracking of Fluid Invasion Using Time-Resolved Neutron Tomography. *Transport in Porous Media*. doi: 10.1007/s11242-018-1055-9
- Jiang, Z., Couples, G. D., Lewis, H., & Mangione, A. (2018). An investigation into preserving spatially-distinct pore systems in multi-component rocks using a fossiliferous limestone example. *Computers & Geosciences*, 116, 1–11.
- Jiang, Z., van Dijke, M., Geiger, S., Ma, J., Couples, G., & Li, X. (2017). Pore network extraction for fractured porous media. *Advances in Water Resources*, 107, 280–289.
- Kaestner, A. P., Trtik, P., Zarebanadkouki, M., Kazantsev, D., Snehota, M., Dobson, K. J., & Lehmann, E. H. (2016). Recent developments in neutron imaging with applications for porous media research. *Solid Earth*, 7(5), 1281–1292.
- Kardjilov, N., Hilger, A., Manke, I., Strobl, M., Dawson, M., Williams, S., & Banhart, J. (2011, 9). Neutron tomography instrument CONRAD at HZB. *Nuclear Instruments and Methods in Physics Research Section A: Accelerators, Spectrometers, Detectors and Associated Equipment*, 651(1), 47–52. Retrieved from <https://www.sciencedirect.com/science/article/pii/S0168900211001458> doi: 10.1016/J.NIMA.2011.01.067
- Maire, E., & Withers, P. J. (2014, 1). Quantitative x-ray tomography. *International Materials Reviews*, 59(1), 1–43. Retrieved from <http://www.tandfonline.com/doi/full/10.1179/1743280413Y.0000000023> doi: 10.1179/1743280413Y.0000000023
- Masschaele, B., Dierick, M., Cnudde, V., Van Hoorebeke, L., Delputte, S., Gilde-meister, A., ... Hillenbach, A. (2004). High-speed thermal neutron tomography for the visualization of water repellents, consolidants and water uptake in sand and lime stones. *Radiation physics and chemistry*, 71(3-4), 807–808.
- Masschaele, B., Dierick, M., Van Hoorebeke, L., Cnudde, V., & Jacobs, P. (2004). The use of neutrons and monochromatic x-rays for non-destructive testing in geological materials. *Environmental Geology*, 46(3-4), 486–492.
- Pak, T., Butler, I. B., Geiger, S., van Dijke, M. I. J., & Sorbie, K. S. (2015, 2). Droplet fragmentation: 3D imaging of a previously unidentified pore-scale process during multiphase flow in porous media. *Proceedings of the National Academy of Sciences of the United States of America*, 112(7), 1947–52. Retrieved from <http://www.ncbi.nlm.nih.gov/pubmed/25646491><http://www.pubmedcentral.nih.gov/articlerender.fcgi?artid=PMC4343173> doi: 10.1073/pnas.1420202112

- Palenstijn, W., Batenburg, K., & Sijbers, J. (2011, 11). Performance improvements for iterative electron tomography reconstruction using graphics processing units (GPUs). *Journal of Structural Biology*, 176(2), 250–253. Retrieved from <https://www.sciencedirect.com/science/article/pii/S1047847711002267> doi: 10.1016/J.JSB.2011.07.017
- Palenstijn, W. J., Bédorf, J., Sijbers, J., & Batenburg, K. J. (2017, 1). A distributed ASTRA toolbox. *Advanced Structural and Chemical Imaging*, 2(1), 19. Retrieved from <http://ascimaging.springeropen.com/articles/10.1186/s40679-016-0032-z> doi: 10.1186/s40679-016-0032-z
- Perfect, E., Cheng, C.-L., Kang, M., Bilheux, H., Lamanna, J., Gragg, M., & Wright, D. (2014, 2). Neutron imaging of hydrogen-rich fluids in geomaterials and engineered porous media: A review. *Earth-Science Reviews*, 129, 120–135. Retrieved from <https://www.sciencedirect.com/science/article/pii/S0012825213002079> doi: 10.1016/J.EARSCIREV.2013.11.012
- Pons, A., David, C., Fortin, J., Stanchits, S., Menéndez, B., & Mengus, J. M. (2011, 3). X-ray imaging of water motion during capillary imbibition: A study on how compaction bands impact fluid flow in Bentheim sandstone. *Journal of Geophysical Research*, 116(B3), B03205. Retrieved from <http://doi.wiley.com/10.1029/2010JB007973> doi: 10.1029/2010JB007973
- Tötzke, C., Kardjilov, N., Manke, I., & Oswald, S. E. (2017, 12). Capturing 3D Water Flow in Rooted Soil by Ultra-fast Neutron Tomography. *Scientific Reports*, 7(1), 6192. Retrieved from <http://www.nature.com/articles/s41598-017-06046-w> doi: 10.1038/s41598-017-06046-w
- Tudisco, E., Andò, E., Cailletaud, R., & Hall, S. A. (2017, 1). TomoWarp2: A local digital volume correlation code. *SoftwareX*, 6, 267–270. Retrieved from <https://www.sciencedirect.com/science/article/pii/S2352711017300511> doi: 10.1016/J.SOFTX.2017.10.002
- Tudisco, E., Hall, S., Athanasopoulos, S., & Hovind, J. (2017). Neutron imaging and digital volume correlation to analyse the coupled hydro-mechanics of geomaterials. *Rivista Italiana di Geotecnica*, 51(4). doi: 10.19199/2017.4.0557-1405.60
- van Aarle, W., Palenstijn, W. J., De Beenhouwer, J., Altantzis, T., Bals, S., Batenburg, K. J., & Sijbers, J. (2015, 10). The ASTRA Toolbox: A platform for advanced algorithm development in electron tomography. *Ultramicroscopy*, 157, 35–47. Retrieved from <https://www.sciencedirect.com/science/article/pii/S0304399115001060> doi: 10.1016/J.ULTRAMIC.2015.05.002
- Youssef, S., Deschamps, H., Dautriat, J., Rosenberg, E., Oughanem, R., Maire, E., & Mokso, R. (2013). In-situ 3D Imaging of Fluid Flow Dynamic in Natural Porous Media by Ultra-fast X-ray Microtomography with Sub-second Temporal Resolution. In *1st international conference on tomography of materials and structures; ictms 2013*.